

# Wind erosion on Mars exposes ideal targets for sample return

Mackenzie Day<sup>1</sup> and William Anderson<sup>2</sup>

<sup>1</sup>University of California Los Angeles

<sup>2</sup>University of Texas at Dallas

November 24, 2022

## Abstract

The Mars 2020 rover will land in Jezero crater, characterize the local geology, and collect samples to be sent back to Earth. Ionizing radiation at the martian surface degrades the complex organic molecules sought by this mission, making it critical to mission success that samples be selected from recently eroded strata minimally exposed to surface radiation. Erosion on modern Mars is driven by wind. We used numerical modeling to identify sites near the rover landing area where recent aeolian erosion has likely occurred. Large eddy simulation of turbulent airflow over topography was coupled with interpretations of the surface geology to characterize wind-driven erosion across the Jezero crater delta deposit. We discuss potential sediment sources that could drive abrasion and calculate the largest grains mobilized by typical winds over the study area. Our results identify several locations likely eroded by recent winds that provide optimal sites for sample collection.

1 **Wind erosion on Mars exposes ideal targets for sample return**

2 **Mackenzie Day<sup>1\*</sup>, William Anderson<sup>2</sup>**

3 <sup>1</sup>University of California Los Angeles, Department of Earth, Planetary, & Space Sciences.

4 <sup>2</sup>The University of Texas at Dallas, Department of Mechanical Engineering.

5

6 \*Corresponding author: Mackenzie Day ([daym@epss.ucla.edu](mailto:daym@epss.ucla.edu))

7

8 **Key Points:**

- 9
- 10 • Large eddy simulation was used to model wind-driven surface shear stress across the  
Jezero crater western delta
  - 11 • Locations of high shear stress correlate with locations of recent aeolian erosion, a key  
12 consideration in sample selection
  - 13 • Based on two previously interpreted wind regimes, recently-exposed strata are discussed  
14 as potential sampling sites

15

16

17

**18 Abstract**

19 The Mars 2020 rover will land in Jezero crater, characterize the local geology, and collect  
20 samples to be sent back to Earth. Ionizing radiation at the martian surface degrades the complex  
21 organic molecules sought by this mission, making it critical to mission success that samples be  
22 selected from recently eroded strata minimally exposed to surface radiation. Erosion on modern  
23 Mars is driven by wind. We used numerical modeling to identify sites near the rover landing area  
24 where recent aeolian erosion has likely occurred. Large eddy simulation of turbulent airflow over  
25 topography was coupled with interpretations of the surface geology to characterize wind-driven  
26 erosion across the Jezero crater delta deposit. We discuss potential sediment sources that could  
27 drive abrasion and calculate the largest grains mobilized by typical winds over the study area.  
28 Our results identify several locations likely eroded by recent winds that provide optimal sites for  
29 sample collection.

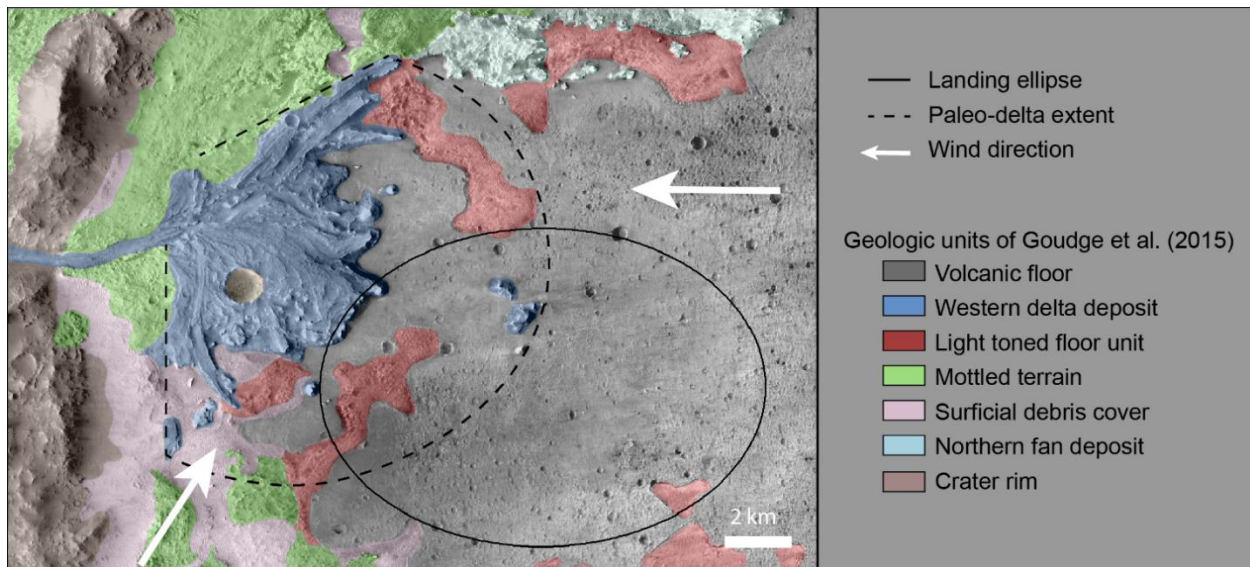
**30 Plain Language Summary**

31 The Mars 2020 rover will land in Jezero crater and collect samples that will eventually be  
32 returned to Earth. Rocks exposed at the surface of Mars become damaged by radiation, therefore,  
33 the best samples to collect will be those that have recently been exposed to the surface. On Mars,  
34 surface erosion is mostly caused by wind. In this work, we use numerical modeling of wind over  
35 the terrain in the Mars 2020 landing area to predict where the landscape has most recently been  
36 eroded and identify potential locations for optimal sample collection.

**37 1 Introduction**

38 The Mars 2020 mission will provide unprecedented information about the geology and  
39 history of Mars with the ultimate goal of selecting samples to be returned to Earth. The planned  
40 landing site in Jezero crater, which includes ancient delta deposits, represents an attractive  
41 location for sampling because of the diverse mineralogy in the study area (Goudge et al., 2015;  
42 Salvatore et al., 2018) and the potential habitability of the crater's ancient lake (Fig. 1; Fassett &  
43 Head, 2005; Schon et al., 2012). Lake and delta sedimentary rocks can preserve complex  
44 biomolecules; therefore, samples collected in Jezero crater will offer an exceptional opportunity  
45 to look for evidence of ancient life on Mars (Ehlmann et al., 2008). However, the fidelity of any  
46 preserved biosignatures will depend on how recently they have been exposed to surface ionizing  
47 radiation (Dartnell et al., 2007, 2014), and the recency of erosional exposure on modern Mars  
48 depends entirely on the wind. Wind has eroded  $\sim 3 \text{ km}^3$  of strata from the Jezero delta deposit  
49 (Goudge et al., 2017), but not uniformly, because turbulent interactions between wind and  
50 topography cause some regions to erode preferentially over others (Anderson & Day, 2017).  
51 Therefore, a thorough understanding of how wind responds to the landscape is essential for  
52 identifying sampling locations that have been recently exposed and have the highest biosignature  
53 preservation potential.

54 To date, orbitally-acquired images have provided a glimpse of the complexity of surface-  
55 wind interactions in the landing area. Previous work on wind-formed surface geology interpreted  
56 two distinct wind regimes that have influenced the landing area (Chojnacki et al., 2018; Day &  
57 Dorn, 2019). Erosional linear features called 'yardangs' cross-cut the crater floor and delta  
58 deposit, reflecting an era in which southwesterly winds eroded the surface and removed delta  
59 strata. Meanwhile, wind streaks and wind-formed bedforms reflect more recent easterly winds.



60  
61  
62 **Figure 1:** Mars 2020 rover landing area in Jezero crater, Mars. The rover *Perseverance* will land just  
63 southeast of a large remnant delta deposit emplaced in an ancient lake. The delta deposit was once  
64 much more extensive (dashed line), but has been eroded by wind. Two wind directions have influenced  
65 the landscape (arrows), and each indicates different potential optimal sampling locations. Geologic  
66 mapping of the area is provided for context.

67  
68 Intuitively, recent winds should dictate the locations of recent erosion. However, the current  
69 supply of sediment in the area is low, and it remains unclear whether modern easterly or older  
70 southwesterly winds are responsible for the observed erosion of the delta deposits.

71 In this work, we leverage computational methods for simulation of realistic turbulent  
72 flow over the delta topography to identify erosion patterns on the delta deposit inferred from two  
73 different wind directions. The results highlight locations of recent erosion where the newly  
74 exposed strata have experienced minimal surface radiation. Samples collected in these areas will  
75 have the highest chance of preserving un-degraded biosignatures. Erosion is only possible when  
76 sediment is available to cause abrasion, and using the simulation results, we further calculate the  
77 largest grain sizes expected to be mobile under typical martian winds. Surface change on modern  
78 Mars is dominated by wind, therefore, considering the context of surface-wind interactions will  
79 be critical to the mission objectives of characterizing the formation and modification of the  
80 geologic record and identifying locations with high potential for preservation of biosignatures.

## 81 **2 Materials and Methods**

82 Large-eddy simulation (LES) was used to model turbulent atmospheric surface layer flow  
83 over topography of the delta proximal to the Mars 2020 landing ellipse. Input topography was  
84 derived from a digital elevation model (DEM) provided by the High Resolution Imaging Science  
85 Experiment (McEwen et al., 2007). To make the computation tractable, the 1 m/px DEM was  
86 down-sampled to a resolution of 100 m/px. Elevation values were clipped to the mapped extent  
87 of the delta deposit with margin to ensure that scarps on the edge of the deposits were captured.  
88 The area beyond the delta was set to a reference elevation for continuity in the model. In one  
89 simulation, the delta was subjected to unidirectional atmospheric forcing from the southwest, and  
90 in the second simulation to forcing from the east. The velocity field is modeled as

91 incompressible, and the viscous stresses are neglected, owing to the very high Reynolds number  
 92 typical of such large-scale flows (Wyngaard, 2010). With this, evolution of velocity is regulated  
 93 by the following system of equations,

$$94 \quad \frac{\partial \tilde{\mathbf{u}}}{\partial t} + \tilde{\mathbf{u}} \cdot \nabla \tilde{\mathbf{u}} = -\frac{1}{\rho} \nabla \tilde{p} - \nabla \cdot \boldsymbol{\tau} + \mathbf{e}_x \Pi + \mathbf{f}_b \quad \text{and} \quad \nabla \cdot \tilde{\mathbf{u}} = 0, \quad (1)$$

95 where  $\tilde{\mathbf{u}}$  is the velocity vector and “tilde” denotes the grid-filtering operation (Pope, 2000),  $\rho$  is  
 96 density,  $\nabla \tilde{p}$  is a pressure correction imposed to maintain the incompressibility condition,  
 97  $\nabla \cdot \tilde{\mathbf{u}} = 0$ ,  $\Pi$  is a pressure correction aligned in the streamwise (x) direction, and  $\mathbf{f}_b$  is a body  
 98 force included to represent the presence of topographic undulations within Jezero crater. The  
 99 LES code was originally used for idealized terrestrial atmospheric boundary layer (ABL)  
 100 turbulence studies (Albertson & Parlange, 1999), but has now been used in a variety of studies,  
 101 including applications to the ABL on Mars (Anderson & Day, 2017; Day et al., 2016). During  
 102 simulation, Equation (1) is solved numerically, with horizontal and vertical gradients assessed in  
 103 Fourier and physical space, respectively. Simulations are advanced until stationarity is attained  
 104 with respect to flow quantities including kinetic energy; the simulations are subsequently  
 105 continued for the purpose of recovering turbulence statistics, which regulate the spatial  
 106 distributions of aerodynamic surface stress used for this article.

107 The body force term,  $\mathbf{f}_b$ , is evaluated using an immersed-boundary method (IBM), which  
 108 has been used in a variety of complementary research efforts in high Reynolds number ASL  
 109 flows over topographic undulations (Anderson, 2013; Anderson & Meneveau, 2010). The grid-  
 110 filtered turbulent stresses,  $\boldsymbol{\tau} = \mathbf{u}' \otimes \mathbf{u}'$ , where  $\mathbf{u}'$  denotes fluctuation from the grid-filtered flow  
 111 (Meneveau & Katz, 2000). In this article,  $\nabla \cdot \boldsymbol{\tau}$  is evaluated with the eddy-viscosity concept; a  
 112 novel closure based open averaging over Lagrangian fluid pathlines is used during LES, which is  
 113 ideal for the present application wherein topographic relief within Jezero induces large-scale  
 114 spatial heterogeneities that preclude averaging based on the existing of spatial homogeneity.

115 To determine an upper bound on the size of grains that would be mobilized by modeled  
 116 winds, we dimensionalized the shear stress distributions following the methods established in the  
 117 authors' previous work (Day et al., 2016). Taking advantage of the definition of shear stress, we  
 118 multiplied the dimensionless basal shear stress output by LES simulations by typical values of  
 119 atmospheric density and surface shear velocity:

$$120 \quad \tau_b = \tau_{LES} \rho_{atm} u_*^2 \quad (2)$$

121 where  $\rho_{atm}$  is the density of the atmosphere, taken as  $0.02 \text{ kg/m}^3$ . The basal shear velocity  
 122 relates to a measured wind speed via the law of the wall:

$$123 \quad u_* = \frac{U(z)\kappa}{\log\left(\frac{z}{z_0}\right)} \quad (3)$$

124 where  $\kappa$  is the von Kármán constant,  $U(z)$  the wind speed at height  $z$ , and  $z_0$  the roughness length  
 125 scale, here taken to be 300  $\mu\text{m}$ . Based on data collected by the InSight lander (Banfield et al.,  
 126 2020), we assume typical martian winds of  $U = 5$  m/s, at the height of  $z = 1.665$  m.

127 Grains move when the wind exceeds a threshold needed to initiate particle motion. On  
 128 Mars, the threshold of motion is much lower if saltation has already begun. The hysteresis  
 129 between initial and continued motion of sand grains on Mars gives rise to a lower threshold of  
 130 motion, approximated analytically as (Kok, 2010):

$$131 \quad u_{*threshold} = c_1 \left( \frac{700}{P} \right)^{\frac{1}{6}} \left( \frac{220}{T} \right)^{\frac{2}{5}} \exp \left( \left( \frac{c_2}{D} \right)^3 + c_3 D^{\frac{1}{2}} - c_4 D \right) \quad (4)$$

132 where  $P$  is the surface pressure, and  $T$  the temperature, here modeled as 200 K and 1000 Pa.  $D$  is  
 133 the grain size of the particle. To determine the largest grain size mobilized by the wind (Fig.  
 134 2c,d), we compare this hysteretic threshold to the shear velocities derived from LES. At each  
 135 grid space, we compared the modeled shear velocity with the curve in Eq. (4) and identified the  
 136 largest value of  $D$  for which  $u_{*LES} > u_{*threshold}$ . Smaller grains are presumed to be mobile as  
 137 well, but the  $D$  values shown in Figure 2 present upper bounds on mobility and lower bounds on  
 138 grains in locations of observed immobility.

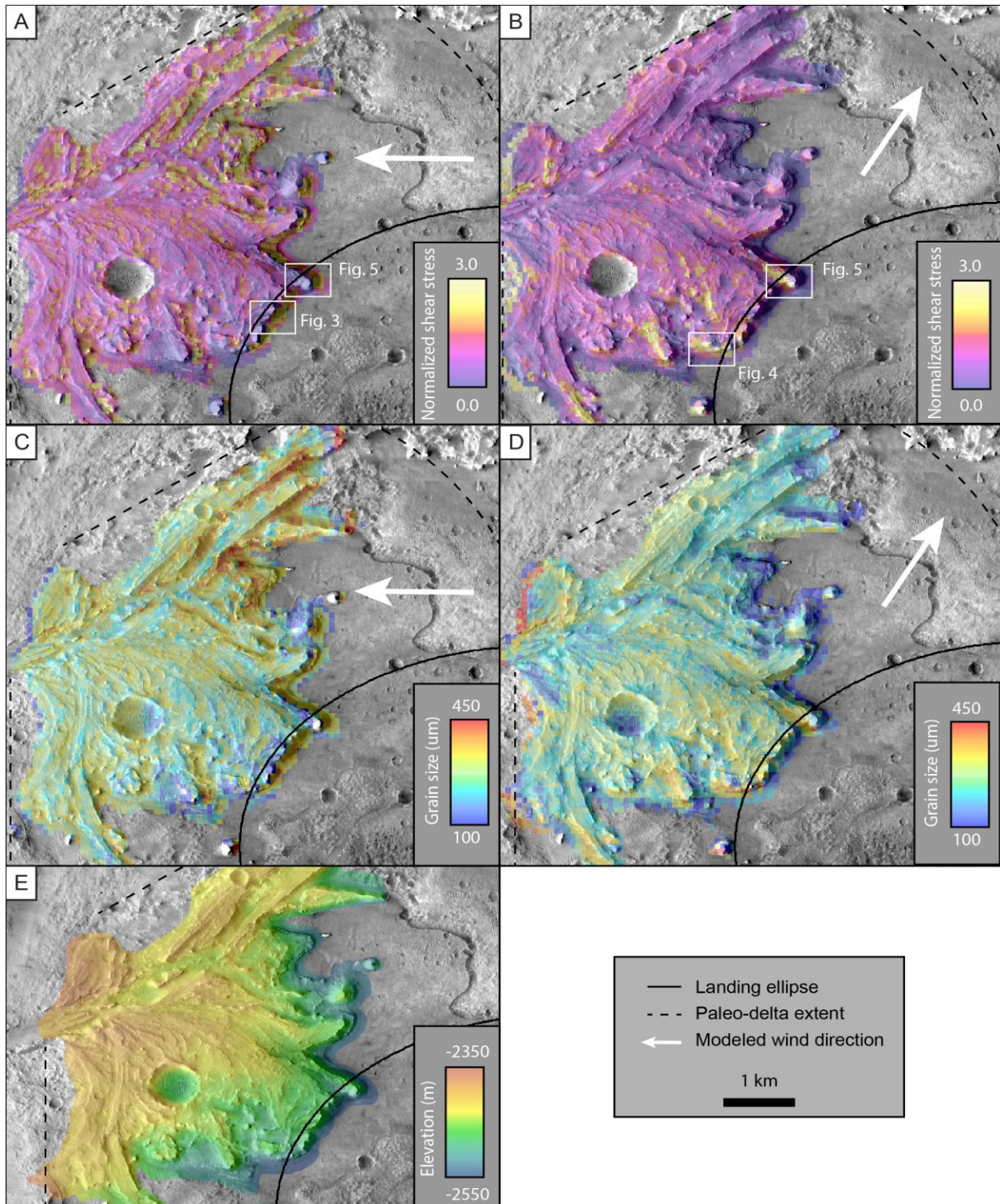
### 139 **3 Results**

#### 140 3.1 Surface stress derived from large eddy simulation

141 Two large eddy simulations were conducted to model turbulent airflow from either the  
 142 east (Fig. 2a) or southwest (Fig. 2b) interacting with the delta topography (Fig. 2e). Simulations  
 143 provided instantaneous vector fields of wind across the delta that can be used to study vorticity,  
 144 shear stress, and turbulent structures. Here, we focus on the imposed surface shear stress as a  
 145 proxy for the tendency of the wind to cause erosion (e.g., Anderson et al., 1991). The magnitude  
 146 of shear stress is proportional to the size of sand grains that can be moved and the volume  
 147 capacity of sediment that can be transported by the wind (e.g., Kok, 2010; Martin & Kok, 2017;  
 148 Shao & Lu, 2000). Erosion occurs when mobile sediment impacts a surface, causing material  
 149 removal by abrasion. Thus, holding rock type, sediment supply, and atmospheric conditions  
 150 constant, shear stress can be used to identify where a surface has been subject to the strongest  
 151 erosion. A map of shear stress is therefore, a proxy map of where strata have been most recently  
 152 exposed. The non-linearities in turbulent flow over complex topography require the use of high-  
 153 fidelity modeling to characterize how wind responds to the surface (Pope, 2000). A time-  
 154 averaged representation of the surface shear stress from the large eddy simulations is shown in  
 155 Figure 2. The shear stress has been normalized by the mean value, such that a value of 1  
 156 represents the mean, time-averaged surface stress for the region, and values  $>1$  represent stresses  
 157 above the mean.

#### 158 3.2 Locations of recent significant erosion

159 The simulations highlight a number of regions where high shear stress indicates that  
 160 recent erosion would have taken place. Shear stress is maximized along steep topography where



161  
 162 **Figure 2:** Shear stress results from large eddy simulation. Patterns of erosion on the delta deposit can be  
 163 interpreted from the surface shear stress (A/B), and largest grain sizes that could be mobilized by typical  
 164 winds (C/D). Large eddy simulation was conducted on the delta deposit topography (E) to model surface  
 165 shear from easterly (A) and southwesterly (B) winds. Several locations of high shear stress (white boxes),  
 166 a proxy erosion potential, are within the landing ellipse. Erosion can only proceed if sand grains are  
 167 moved by the wind. Estimates of mobile grain sizes derived from the simulations suggest medium-grained  
 168 sand could be mobilized across much of the delta front (C/D).

169 the front of the eroded delta deposit meets the basal plains. These upwind-facing slopes,  
170 therefore, represent locations where erosion would have had the potential to be most rapidly  
171 occurring when the modeled wind was present. However, wind-driven erosion requires available  
172 sediment; mobile sands, not the air itself, are responsible for the actual erosion by abrasion  
173 (Powers, 1936; Suzuki & Takahashi, 1981). Actively migrating sands are relatively rare within  
174 Jezero crater, but locations where active transport has been documented coincide with the high-  
175 shear stress regions modeled in this work (Chojnacki et al., 2018). We used the results of the  
176 large eddy simulation to determine the largest grain sizes mobilized by typical winds on Mars. In  
177 the regions of highest shear stress, we found that wind is expected to mobilize medium-grained  
178 sand (Figs. 2c,d). Satellite imaging has shown changes in the dark sands at the delta front  
179 (Chojnacki et al., 2018). Assuming these sands are similar in grain-size to active sands imaged  
180 by the Mars Science Laboratory rover (i.e., fine to medium; Weitz et al., 2018), results of this  
181 work suggest these grains are likely mobile in typical martian winds.

182 Areas of high shear stress are spread across the delta, but those far from the landing  
183 ellipse present practical difficulties by requiring a further rover traverse. For this reason, below  
184 we discuss three specific areas of high shear stress that are 1) near sediments that could be  
185 entrained by wind to cause modern abrasion, and 2) within or close to within the landing ellipse  
186 (Figs. 3-5).

## 187 **4 Discussion**

### 188 4.1 Sediment availability and traversability hazards

189 Aeolian erosion only occurs when mobile sand is present (Powers, 1936; Suzuki &  
190 Takahashi, 1981). In Jezero crater, two types of bedforms could potentially provide sands and  
191 enable wind-driven erosion. The dominant bedforms in the study area and Jezero crater at large  
192 are straight-crested transverse aeolian ridges (Berman et al., 2011; Zimbelman, 2010). These  
193 bright-looking bedforms are commonly found in topographic lows and are decameters in length.  
194 The second type of bedforms in the study area are “large martian ripples” (Lapotre et al., 2016,  
195 2018). These meter-scale bedforms develop more complex patterns than their straight-crested  
196 neighbors, and are typically dark in satellite images. Unlike the larger bright bedforms that occur  
197 as separated and parallel features, the dark ripples occur on sand sheets with continuous  
198 coverage. Previous research has shown that these dark ripples are actively being transported by  
199 the wind (Chojnacki et al., 2018). Conversely, the bright bedforms appear inactive and have not  
200 changed position in the last ~10 years. This inactivity suggests that the sand in these bedforms is  
201 not available to be entrained by the wind, and even though the bright bedforms are abundant,  
202 they may not provide sediment for erosion. Grain size distributions within or armoring the  
203 bedforms could account for the apparent differences in activity over time. The grain size values  
204 shown in Figure 2 provide upper limits on the grains in mobile bedforms, and lower limits on the  
205 surface grains of immobile bedforms.

206 Bedforms in the study area also present a practical difficulty for the rover. Dunes, ripples,  
207 and related accumulations of sand can be difficult for wheeled rovers to traverse. The two Mars  
208 Exploration Rovers, *Opportunity* and *Spirit*, both became trapped in wind-blown ripples,  
209 ultimately ending the mission of *Spirit* (Greeley et al., 2008; Sullivan et al., 2005). The Mars  
210 Science Laboratory rover *Curiosity* also encountered mobility issues in wind-blown bedforms  
211 (Rothrock et al., 2016), but was able to traverse a large bright bedform with little difficulty

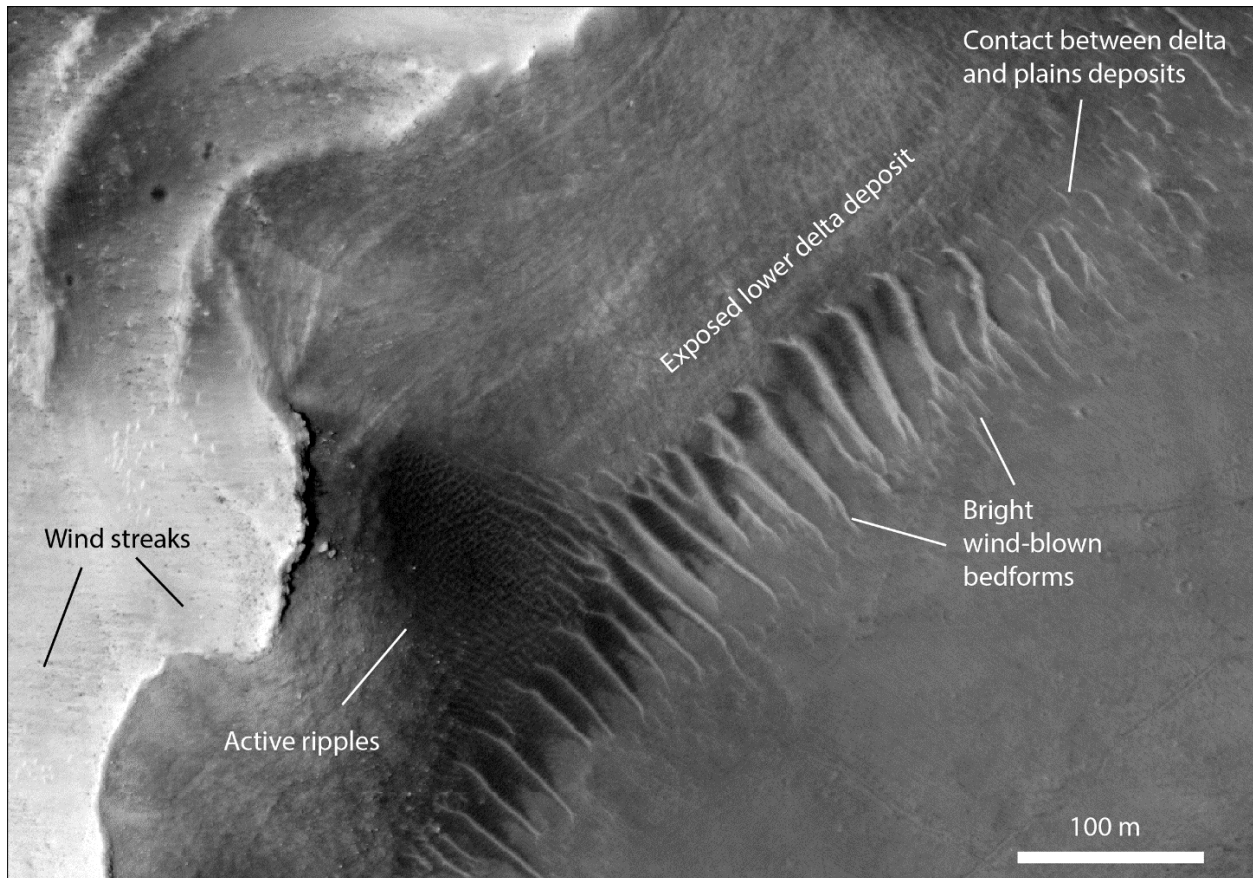


**Figure 3: Lower delta deposits exposed by strongly erosive easterly winds.** Layered strata from the delta deposit are evident on the sloping surface above smooth plains covered in active and inactive bedforms that concentrate near the change in topography. Here the contact between the delta and plains deposits could be accessed by a rover. ESP\_042315\_1985.

212  
213  
214  
215  
216  
217

218 (Arvidson et al., 2017). The aeolian bedforms in Jezero crater share characteristics with the  
219 bedforms that challenged the *Curiosity* rover and the bedform it traversed, making the  
220 trafficability of these features uncertain. Regardless, understanding wind-blown sands as both a  
221 scientific tool and an engineering hazard will be critical to successfully collecting samples that  
222 optimize the chances of detecting ancient martian life.

#### 223 4.2 Optimal sampling sites for Mars Sample Return

224 Based on the results of large eddy simulations, three areas near the rover landing ellipse  
225 have experienced high shear stresses, and are locations where strata may have been recently  
226 exposed by easterly or southwesterly winds. To date, it remains unclear which winds have most  
227 recently eroded material from the delta deposit. Given the amount of material interpreted to have  
228 been removed (Goudge et al., 2017), it is expected that upon landing the rover will encounter a  
229 landscape that has been highly abraded. The millimeter- to decimeter-scale patterns of this  
230 abrasion, not resolvable in satellite images, will provide evidence of sand-transporting, erosive  
231 winds and will enable differentiation between the models shown here (Bridges et al., 2004,  
232 2014).

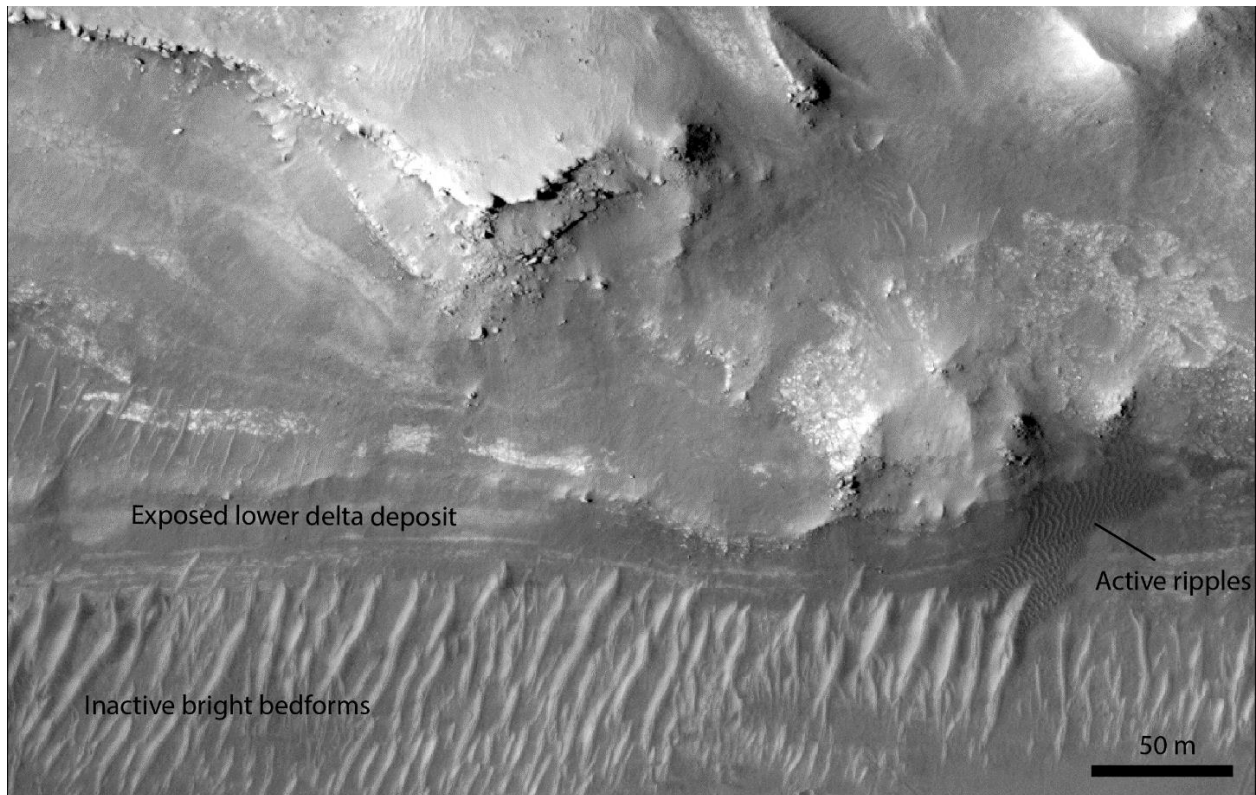
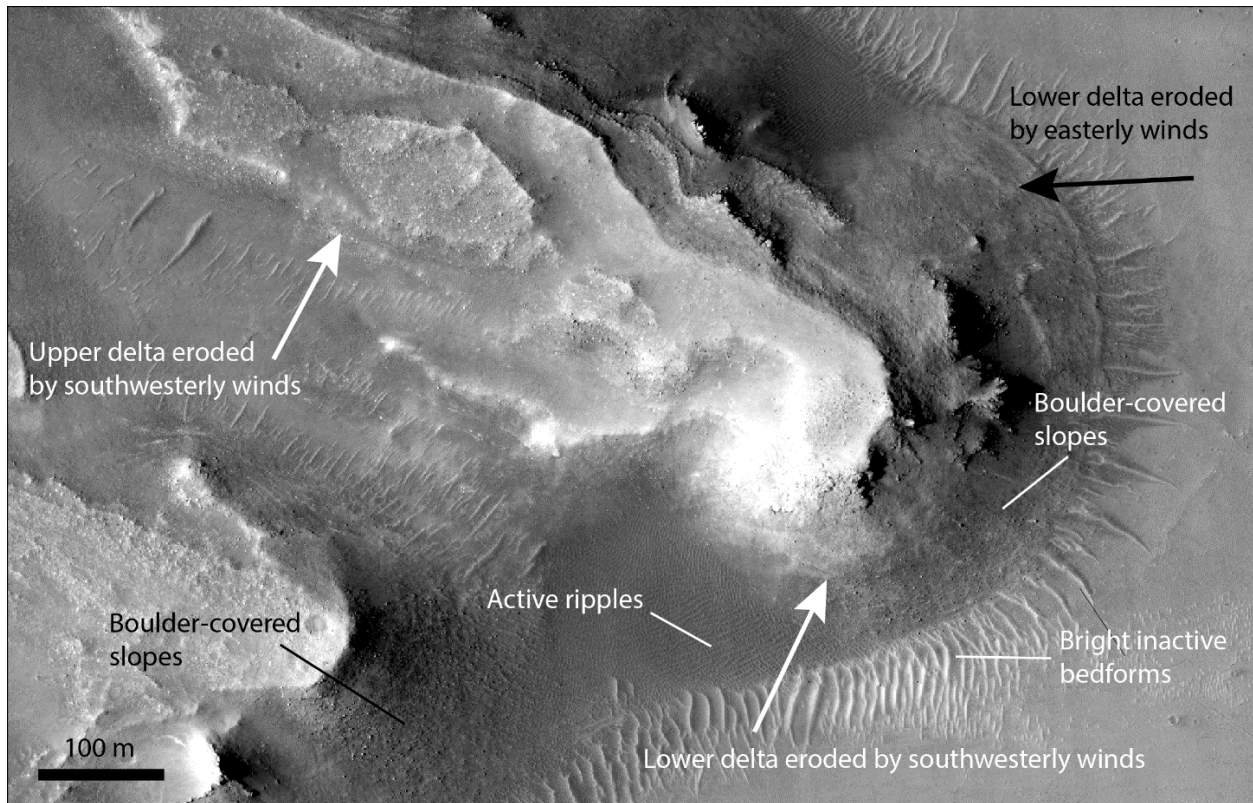


**Figure 4: Lower delta deposits exposed by strongly erosive southwesterly winds.** Lower delta strata exposed in this area show striking light-toned layers. Active and inactive bedforms cover the smooth plains at the base of the slope. ESP\_037396\_1985.

233  
234  
235  
236  
237

238 A high-priority target for sampling will be the basal strata in the delta deposit. Although  
239 material higher in the delta is also of interest, basal and distal portions of the deposit are most  
240 likely to house any fine-grained organic material emplaced during the formation of the delta.  
241 Figure 3 shows basal delta deposits exposed on a slope that would have experienced high surface  
242 stresses from easterly winds. Layering in this slope is juxtaposed with active sands from a small  
243 ripple field climbing the exposed face. Dark and light bedforms impede slope access, but  
244 bedrock can be seen between the larger straight-crested bedforms. In the northeast portion of this  
245 potential sampling area, the bedforms become sparser and delta strata can be followed from the  
246 deposit to the contact with the underlying plains, thus providing confidence that the delta strata  
247 could be easily accessed by the rover. On the upper surface of the delta, thin wind streaks record  
248 easterly winds, consistent with previous works.

249 Basal delta deposits are also exposed on a face that would be eroded under southwesterly  
250 winds (Fig. 4). Again, active and inactive bedforms are juxtaposed at the base of the deposit,  
251 suggesting that some sediment would be available to cause erosion. Strata within the deposit  
252 include light-tone beds, potentially associated with clay minerals previously identified in the  
253 region (Ehlmann et al., 2008; Goudge et al., 2015). A field of inactive light bedforms sits along  
254 the base of the exposed face, obscuring the transition from delta strata to plains. Bedforms in this  
255 area are more varied in size, obscuring more of the inter-bedform space and potentially posing  
256 difficulties for mobility.



257  
 258 **Figure 5: Delta strata eroded by easterly and southwesterly winds in close proximity.** This  
 259 protruding outcrop of delta strata includes areas that would have been rapidly eroded by southwesterly  
 260 winds (white arrows) and easterly winds (black arrow). Both lower and upper delta strata are accessible  
 261 here. Active and inactive bedforms are present along the base of the slope. Boulders and loose cover  
 262 obscure the strata in the slope itself. ESP\_037330\_1990.

263  
 264 Given that it remains unclear which winds caused the most recent erosion, there are  
 265 practical benefits to locations where strata are exposed in multiple orientations. Such locations  
 266 also provide opportunities to observe the three-dimensional geometry of the delta. The region  
 267 shown in Figure 5 includes portions of the delta deposit that experience high surface shear  
 268 stresses from both easterly and southwesterly winds (Fig. 2). As elsewhere, dark, active ripples  
 269 are juxtaposed with bright bedforms at the base of the delta deposit. The large bedforms are  
 270 oriented normal to the slope, such that a rover could drive between bedforms, however, bedform  
 271 spacing and inter-bedform sediment cover varies, with sediment cover decreasing to the north.  
 272 This location provides access to both lower and upper strata in the delta deposit. In the  
 273 simulation of southwesterly winds, both lower and upper delta strata experience high surface  
 274 shear stresses. Lower delta strata in this area are less clearly exposed. Boulders on the slope  
 275 suggest mass wasting; material from the overlying units may cover the lowermost strata. This is  
 276 counter to the idea that this material has been recently eroded by wind. The goal of this work is  
 277 not to identify a perfect target for exploration, but rather to discuss the available options in the  
 278 context of surface-wind interactions.

#### 279 4. 3 Geology augmenting meteorology

281 Measurements of the modern wind will be collected by the Mars Environmental  
 282 Dynamics Analyzer (MEDA) onboard the *Perseverance* rover (Rodriguez-Manfredi et al., 2014).

283 Although these measurements will provide a helpful characterization of the local turbulent  
284 winds, measurements from MEDA alone are insufficient to identify locations of recent erosion.  
285 Erosion requires mobile sand, and the threshold wind speeds at which sand saltation is initiated  
286 on Mars are not fully understood (Baker et al., 2018; Kok, 2010; Sullivan & Kok, 2017). Day-to-  
287 day winds in Jezero crater may or may not transport sediment, and even if daily winds can be  
288 demonstrated to move sand, the current availability of sediment may not be sufficient to cause  
289 erosion. Furthermore, winds vary in speed and direction both spatially and temporally (Day &  
290 Rebolledo, 2019; Haberle et al., 1993; Leovy & Mintz, 1969; Thomas & Veverka, 1979). It will  
291 take the full duration of the primary mission to characterize the seasonal variations in surface  
292 winds using MEDA, and to determine whether and where modern winds cause erosion. By that  
293 time, any results will be too late to be applied to mission planning and sample site selection.  
294 Therefore, basing interpretations and sampling decisions on the observed surface geology, which  
295 necessarily reflects sand-transporting winds, will provide a rapid and rigorous characterization of  
296 the recent wind history critical to identifying recently exposed outcrops and maximizing the  
297 potential to identify evidence of early life on Mars.

298

## 299 **Acknowledgments**

300 The authors thank Kate Ledger for editorial contributions to this work. Data availability  
301 statement: Data used in this work is archived online at [https://github.com/GALE-Lab/Day-](https://github.com/GALE-Lab/Day-Anderson-SubmittedToGRL)  
302 [Anderson-SubmittedToGRL](https://github.com/GALE-Lab/Day-Anderson-SubmittedToGRL).

303

## 304 **References**

305

- 306 Albertson, J. D., & Parlange, M. B. (1999). Surface length scales and shear stress: Implications  
307 for land-atmosphere interaction over complex terrain. *Water Resources Research*, 35(7),  
308 2121–2132.
- 309 Anderson, R. S., Sørensen, M., & Willetts, B. B. (1991). A review of recent progress in our  
310 understanding of aeolian sediment transport. In *Aeolian Grain Transport 1* (pp. 1–19).  
311 Springer.
- 312 Anderson, W. (2013). An immersed boundary method wall model for high-Reynolds-number  
313 channel flow over complex topography. *International Journal for Numerical Methods in*  
314 *Fluids*, 71(12), 1588–1608.
- 315 Anderson, W., & Day, M. (2017). Turbulent flow over craters on Mars: Vorticity dynamics  
316 reveal aeolian excavation mechanism. *Physical Review E*, 96(4), 43110. Retrieved from  
317 <https://link.aps.org/doi/10.1103/PhysRevE.96.043110>
- 318 Anderson, W., & Meneveau, C. (2010). A large-eddy simulation model for boundary-layer flow  
319 over surfaces with horizontally resolved but vertically unresolved roughness elements.  
320 *Boundary-Layer Meteorology*, 137(3), 397–415.
- 321 Arvidson, R. E., Iagnemma, K. D., Maimone, M., Fraeman, A. A., Zhou, F., Heverly, M. C., et  
322 al. (2017). Mars Science Laboratory Curiosity rover megaripple crossings up to sol 710  
323 in Gale Crater. *Journal of Field Robotics*, 34(3), 495–518.
- 324 Baker, M. M., Newman, C. E., Lapotre, M. G. A., Sullivan, R., Bridges, N. T., & Lewis, K. W.  
325 (2018). Coarse Sediment Transport in the Modern Martian Environment. *Journal of*

- 326 Geophysical Research: Planets, 123(6), 1380–1394.  
327 <https://doi.org/10.1002/2017JE005513>
- 328 Banfield, D., Spiga, A., Newman, C., Forget, F., Lemmon, M., Lorenz, R., et al. (2020). The  
329 atmosphere of Mars as observed by InSight. *Nature Geoscience*, 1–9.
- 330 Berman, D. C., Balme, M. R., Rafkin, S. C. R., & Zimbelman, J. R. (2011). Transverse aeolian  
331 ridges (TARs) on Mars II: distributions, orientations, and ages. *Icarus*, 213(1), 116–130.
- 332 Bridges, N. T., Laity, J. E., Greeley, R., Phoreman, J., & Eddlemon, E. E. (2004). Insights on  
333 rock abrasion and ventifact formation from laboratory and field analog studies with  
334 applications to Mars. *Planetary and Space Science*, 52(1), 199–213.  
335 <https://doi.org/10.1016/j.pss.2003.08.026>
- 336 Bridges, N. T., Kocurek, G. A., Langevin, Y., Lewis, K. W., Mangold, N., Maurice, S., et al.  
337 (2014). The rock abrasion record at Gale Crater: Mars Science Laboratory results from  
338 Bradbury Landing to Rocknest. *Journal of Geophysical Research - Planets*, 119(6), 1374–  
339 1389. <https://doi.org/10.1002/2013je004579>
- 340 Chojnacki, M., Banks, M., & Urso, A. (2018). Wind-Driven Erosion and Exposure Potential at  
341 Mars 2020 Rover Candidate-Landing Sites. *Journal of Geophysical Research: Planets*,  
342 123(2), 468–488.
- 343 Dartnell, L. R., Desorgher, L., Ward, J. M., & Coates, A. J. (2007). Modelling the surface and  
344 subsurface Martian radiation environment: Implications for astrobiology. *Geophysical  
345 Research Letters*, 34(2), L02207. <https://doi.org/10.1029/2006gl027494>
- 346 Dartnell, L. R., Patel, M. R., Cockell, C., Burchell, M., & Martins, Z. (2014). Degradation of  
347 microbial fluorescence biosignatures by solar ultraviolet radiation on Mars. *International  
348 Journal of Astrobiology*, 13(2), 112–123. <https://doi.org/10.1017/s1473550413000335>
- 349 Day, M., & Dorn, T. (2019). Wind in Jezero crater, Mars. *Geophysical Research Letters*, 46(6),  
350 3099–3107.
- 351 Day, M., & Rebolledo, L. (2019). Intermittency in Wind-Driven Surface Alteration on Mars  
352 Interpreted From Wind Streaks and Measurements by InSight. *Geophysical Research  
353 Letters*, 46(22), 12747–12755.
- 354 Day, M., Anderson, W., Kocurek, G., & Mohrig, D. (2016). Carving intracrater layered deposits  
355 with wind on Mars. *Geophysical Research Letters*, 43(6), 2473–2479.  
356 <https://doi.org/10.1002/2016gl068011>
- 357 Ehlmann, B. L., Mustard, J. F., Fassett, C. I., Schon, S. C., Head III, J. W., Marais, D. J. Des, et  
358 al. (2008). Clay minerals in delta deposits and organic preservation potential on Mars.  
359 *Nature Geoscience*, 1(6), 355–358.
- 360 Fassett, C. I., & Head, J. W. (2005). Fluvial sedimentary deposits on Mars: Ancient deltas in a  
361 crater lake in the Nili Fossae region. *Geophysical Research Letters*, 32(14).
- 362 Greeley, R., Whelley, P. L., Neakrase, L. D. V., Arvidson, R. E., Bridges, N. T., Cabrol, N. A., et  
363 al. (2008). Columbia Hills, Mars: Aeolian features seen from the ground and orbit.  
364 *Journal of Geophysical Research - Planets*, 113(E6).
- 365 Goudge, T. A., Mustard, J. F., Head, J. W., Fassett, C. I., & Wiseman, S. M. (2015). Assessing  
366 the mineralogy of the watershed and fan deposits of the Jezero crater paleolake system,  
367 Mars. *Journal of Geophysical Research: Planets*, 120(4), 775–808.
- 368 Goudge, T. A., Mohrig, D., Cardenas, B. T., Hughes, C. M., & Fassett, C. I. (2017). Stratigraphy  
369 and Evolution of Delta Channel Deposits, Jezero Crater, Mars.
- 370 Haberle, R. M., Pollack, J. B., Barnes, J. R., Zurek, R. W., Leovy, C. B., Murphy, J. R., et al.  
371 (1993). Mars atmospheric dynamics as simulated by the NASA Ames General

- 372 Circulation Model: 1. The zonal-mean circulation. *Journal of Geophysical Research:*  
373 *Planets*, 98(E2), 3093–3123.
- 374 Kok, J. F. (2010). An improved parameterization of wind-blown sand flux on Mars that includes  
375 the effect of hysteresis. *Geophysical Research Letters*, 37(12).  
376 <https://doi.org/10.1029/2010gl043646>
- 377 Kok, J. F. (2010). Analytical calculation of the minimum wind speed required to sustain wind-  
378 blown sand on Earth and Mars. *Geophysical Research Letters*, 37(L12202).
- 379 Lapotre, M. G. A., Ewing, R. C., Lamb, M. P., Fischer, W. W., Grotzinger, J. P., Rubin, D. M.,  
380 et al. (2016). Large wind ripples on Mars: A record of atmospheric evolution. *Science*,  
381 353(6294), 55–58. <https://doi.org/10.1126/science.aaf3206>
- 382 Lapotre, M. G. A., Ewing, R. C., Weitz, C. M., Lewis, K. W., Lamb, M. P., Ehlmann, B. L., &  
383 Rubin, D. M. (2018). Morphologic diversity of Martian ripples: Implications for  
384 large-ripple formation. *Geophysical Research Letters*, 45(19), 10–229.
- 385 Leovy, C., & Mintz, Y. (1969). Numerical simulation of the atmospheric circulation and climate  
386 of Mars. *Journal of the Atmospheric Sciences*, 26(6), 1167–1190.
- 387 Martin, R. L., & Kok, J. F. (2017). Wind-invariant saltation heights imply linear scaling of  
388 aeolian saltation flux with shear stress. *Science Advances*, 3(6).  
389 <https://doi.org/10.1126/sciadv.1602569>
- 390 McEwen, A. S., Eliason, E. M., Bergstrom, J. W., Bridges, N. T., Hansen, C. J., Delamere, W.  
391 A., et al. (2007). Mars Reconnaissance Orbiter's High Resolution Imaging Science  
392 Experiment (HiRISE). *Journal of Geophysical Research: Planets*, 112(E5).  
393 <https://doi.org/10.1029/2005je002605>
- 394 Meneveau, C., & Katz, J. (2000). Scale-invariance and turbulence models for large-eddy  
395 simulation. *Annual Review of Fluid Mechanics*, 32(1), 1–32.  
396 <https://doi.org/10.1146/annurev.fluid.32.1.1>
- 397 Pope, S. B. (2000). *Turbulent flows*. Cambridge: Cambridge University Press.
- 398 Powers, W. E. (1936). The evidences of wind abrasion. *The Journal of Geology*, 44(2, Part 1),  
399 214–219.
- 400 Rodriguez-Manfredi, J. A., de la Torre, M., Conrad, P., Lemmon, M., Martinez, G., Newman, C.,  
401 et al. (2014). MEDA: an environmental and meteorological package for Mars 2020. In  
402 *Lunar and Planetary Science Conference (Vol. 45, p. 2837)*.
- 403 Rothrock, B., Kennedy, R., Cunningham, C., Papon, J., Heverly, M., & Ono, M. (2016). Spoc:  
404 Deep learning-based terrain classification for mars rover missions. In *AIAA SPACE*  
405 2016 (p. 5539).
- 406 Salvatore, M. R., Goudge, T. A., Bramble, M. S., Edwards, C. S., Bandfield, J. L., Amador, E.  
407 S., et al. (2018). Bulk mineralogy of the NE Syrtis and Jezero crater regions of Mars  
408 derived through thermal infrared spectral analyses. *Icarus*, 301, 76–96.
- 409 Schon, S. C., Head, J. W., & Fassett, C. I. (2012). An overfilled lacustrine system and  
410 progradational delta in Jezero crater, Mars: Implications for Noachian climate. *Planetary*  
411 *and Space Science*, 67(1), 28–45.
- 412 Shao, Y., & Lu, H. (2000). A simple expression for wind erosion threshold friction velocity.  
413 *Journal of Geophysical Research*, 105(D17), 22437–22443.  
414 <https://doi.org/10.1029/2000jd900304>
- 415 Sullivan, R., & Kok, J. F. (2017). Aeolian saltation on Mars at low wind speeds. *Journal of*  
416 *Geophysical Research: Planets*, 122(10), 2111–2143.  
417 <https://doi.org/10.1002/2017je005275>

- 418 Sullivan, R., Banfield, D., Bell, J., Calvin, W., Fike, D., Golombek, M., et al. (2005). Aeolian  
419 processes at the Mars Exploration Rover Meridiani Planum landing site. *Nature*,  
420 436(7047), 58–61. <https://doi.org/10.1038/nature03641>
- 421 Suzuki, T., & Takahashi, K. (1981). An experimental study of wind abrasion. *The Journal of*  
422 *Geology*, 89(1), 23–36.
- 423 Thomas, P., & Veverka, J. (1979). Seasonal and secular variation of wind streaks on Mars: An  
424 analysis of Mariner 9 and Viking data. *Journal of Geophysical Research: Solid Earth*,  
425 84(B14), 8131–8146.
- 426 Weitz, C. M., Sullivan, R. J., Lapotre, M. G. A., Rowland, S. K., Grant, J. A., Baker, M., &  
427 Yingst, R. A. (2018). Sand grain sizes and shapes in eolian bedforms at Gale crater,  
428 Mars. *Geophysical Research Letters*, 45(18), 9471–9479.
- 429 Wyngaard, J. C. (2010). *Turbulence in the Atmosphere*. Cambridge University Press.
- 430 Zimbelman, J. R. (2010). Transverse Aeolian Ridges on Mars: First results from HiRISE images.  
431 *Geomorphology*, 121(1), 22–29. <https://doi.org/10.1016/j.geomorph.2009.05.012>
- 432
- 433